Volume 15, Issue 2, 152523 (1-12)

Iranian Journal of Catalysis (IJC)

https://doi.org/10.57647/j.ijc.2025.1502.23

A nanoporous metal organic framework/GO hybrid for photodegradation under visible light

Sedigheh Rahimi Khomami, Afshin Pourahmad*, Mohammad Nikpassand

Department of Chemistry, Rasht Branch, Islamic Azad University, Rasht, Iran.

***Corresponding author:** pourahmad@iaurasht.ac.ir

Original Research

Received:
3 February 2025
Revised:
27 March 2025
Accepted:
20 April 2025
Published online:
30 April 2025

© 2025 The Author(s). Published by the OICC Press under the terms of the Creative Commons Attribution License, which permits use, distribution and reproduction in any medium, provided the original work is properly cited.

Abstract:

Metal-organic frameworks (MOFs) show promise for photocatalytic applications; however, they encounter challenges related to stability and conductivity. Researchers are prioritizing the development of composite materials, specifically through the integration of graphene oxide (GO) with MOFs, to enhance their performance and address these limitations. In this investigation, GO was synthesized via the Staudenmeier method. The metal-organic framework, designated as MOF-199(Cu), was synthesized using the wet impregnation method at ambient temperature, employing copper (II) acetate monohydrate as the copper precursor and benzene tricarboxylic acid as the linker. The MOF-199/GO nanocomposite was subsequently prepared using the hydrothermal method at room temperature. The photocatalytic activity of the nanocomposite was systematically evaluated by assessing its ability to degrade Rhodamine B (RhB) as a cationic dye, under visible light irradiation. Characterization of the synthesized materials was conducted using various spectroscopy techniques. SEM and TEM images confirmed the presence of well-dispersed and isolated forms of MOF-199 particles on the GO substrate. The X-ray diffraction pattern showed that the structures of GO and MOF-199 in the nanocomposite have not changed. The DRS results indicated that the MOF-199/GO nanocomposite is a promising photocatalyst for the degradation of RhB when subjected to visible light irradiation. With the incorporation of GO, the MOF-199/GO nanocomposite with GO content of 10 wt% exhibited enhanced degradation of RhB dye compared to MOF or GO individually. The superior photocatalytic performance of the composite was attributed to the synergistic effects resulting from the MOF-199 structure. Furthermore, the MOF-199/GO photocatalyst demonstrated remarkable stability, showing no significant loss of photocatalytic activity over five cycles, suggesting its potential for repeated use in photocatalytic applications.

Keywords: Graphene oxide; Photocatalyst; MOF; Nanocomposites; Rhodamine B

1. Introduction

In recent decades, the pollution from industrial wastewater and its high toxicity have caused water and environmental contamination [1]. Organic pollutants, despite their low concentration, are harmful due to their persistence and resistance to degradation. The dyes in water pose a threat to plants and animals, leading to carcinogenic effects, birth defects, and hormonal imbalances in humans [2]. Various techniques have been employed so far to degrade dyes in water [3, 4]. Among which, photocatalytic degradation has been demonstrated to be one of the most efficient techniques, with environmental sustainability, low cost, high efficiency, and wide applicability [5, 6]. So far, a diverse array of photocatalysts has been extensively developed for photocatalytic applications, such as TiO_2, MSM-4s, SiO_2, zeolites, and MOFs [7–9]. Semiconducting-based photocatalysis is an efficient technology that has been widely used for the degradation/mineralization of organic/inorganic compounds and even for the reduction of some hazardous heavy metals or the degradation of pollutants. In this heterogeneous process, when a semiconducting material is irradiated by suitable photons with an energy photon equal to or greater than the energy gap (Eg) of the semiconductor, commonly in the UV and visible regions of the light, the electron and hole (e^-/h^+) pairs can be induced in the conduction band (CB) and valence band (VB) of the semiconductor, respectively. The e^-/h^+ pairs can, directly and indirectly, participate in the degradation of the subjected pollutant. The photoinduced electrons are potent reducing agents that can begin the degradation of the pollutant via the reduction process. In contrast, the photoinduced holes are the potent oxidizing

agents that can directly attack the organic pollutants and oxidize them to begin the degradation process. In an indirect way, the photoinduced electrons can reduce the dissolved oxygen to yield the powerful reactive superoxide radicals. In contrast, the photoinduced holes can attack the water molecules or hydroxyl anions to yield hydroxyl radicals as powerful oxidizing agents. These powerful reactive radicals can effectively attack the organic molecules and degrade them into smaller intermediates. Further attacks on these intermediates mineralize them into water, carbon dioxide, and other inorganic species. Overall, in semiconducting-based photocatalysis, four main reactive species of the photogenerated electrons and holes, superoxide and hydroxyl radicals, are responsible for degrading the molecules of the pollutants into harmless intermediates, water, carbon dioxide, etc [10]. Metal organic frameworks are a class of materials constructed using a combination of metal ions and organic linkers [11, 12]. Recently, MOFs have gained significant attention as a new type of nanoporous material due to their unique advantages, including tenability, high surface area, functionality, porosity, structural diversity, flexibility, and physicochemical properties in the presence of unsaturated metal sites. This enables customized properties for various applications, including gas storage, drug delivery, energy conversion, sensing, catalysis, photocatalytic applications, and more [13–15]. In pure MOF structures, weak dispersive forces create voids and free spaces between nanocrystals that impact their capacity to retain small molecules. So, the low stability and inadequate mechanical property of most MOFs have restricted their practical applications [16, 17]. Although MOFs have shown significant potential as adsorbents and photocatalysts remediation, to address these shortcomings, MOFs have been combined with various functional materials, such as zeolites, metal oxide nanoparticles, carbon quantum dots, graphene, graphene-oxide and others, to develop metal organic framework-based nanocomposites, which not only limit the disadvantages of MOFs but also achieve synergistic properties [18–20]. MOF composites often exhibit synergic advantages, including reduced band gap energy, decreased photoluminescence, and enhanced photocurrent response, which enable them to capture light energy more efficiently and minimize electron-hole recombination. These improvements make the composites of MOFs with graphene oxide highly effective in utilizing light energy from both visible and ultraviolet regions, with greater stability under harsh conditions compared with pure MOFs [21–23]. As a result, composites have demonstrated remarkable photocatalytic activity in degrading organic pollutants. This is due to the presence of semiconductor materials in the composites, which facilitate electron transfer within the MOF structure and promote the efficient separation of photogenerated electron-hole pairs [24–26]. Graphene oxide is a kind of two-dimensional, hexagonal-shaped nanomaterial characterized by functional groups like carboxyl, hydroxyl, and epoxy. The unique layered structure allows it to function as an adsorbent for various contaminants in aqueous solution. When GO is integrated with metal organic frameworks, the oxygen-rich groups in graphene oxide can interact with the metal ions in metal organic frameworks, creating metal organic framework/graphene oxide nanocomposites [27, 28]. Using of GO in MOF formation offers several benefits, including enhanced interactions within the MOFs and controlled structure growth. The hydrophilic nature of GO allows for easy dispersion in an aqueous environment, which facilitates the creation of new pore spaces at the interface between the MOF blocks and graphene oxide. This increases dispersive forces and helps to retain guest molecules. The combination of MOFs and a dense layer of graphene oxide merges the advantages of both materials, porosity, and electron conductivity of the composites, and enhances the stability [10, 13, 29].

Rhodamine B is a widely used cationic fluorescent dye in various applications such as textiles, food products, scientific investigations, and pharmaceuticals [30, 31]. Various substrates have been evaluated for their efficiency in dye adsorption from wastewater such as alumina oxides [32], carbon-based materials [33], modified 1-hydroxybenzotriaz ole (HBT) [34], carbon nanotubes (CNT) [35], porous silica beads [36], Fe_3O_4@L-arginine [37], and graphene oxide (GO) [38], and Cu-MOF [39]. Existing adsorbents are often costly and challenging to handle or regenerate after applying [40, 41]. Consequently, MOF/GO-based nanocomposites represent promising materials for dye adsorption, due to their ease of surface modification, low toxicity, and extensive surface area. The cationic dye (RhB) exhibits superior adsorption on graphene oxide owing to strong interactions from negatively charged oxygenated functional groups [42–44]. Due to the low conductivity of MOF-199 (Fig. 1), it is commonly integrated with carbon-based materials to improve its porosity and extensive surface area

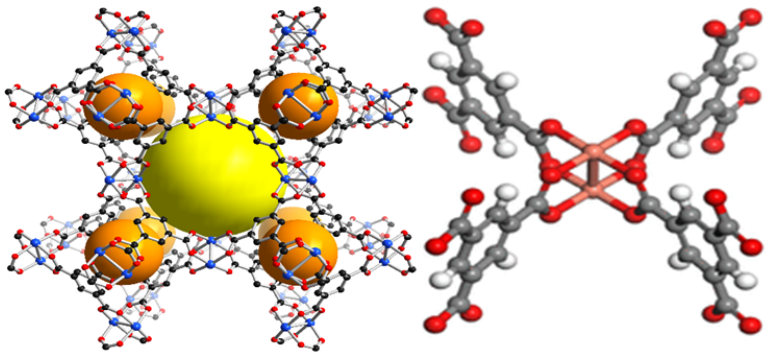

Figure 1. Paddle wheel structure of MOF-199.

while simultaneously enhancing its conductivity [45–48]. Graphene and graphene oxide undergo chemical modifications through covalent and non-covalent bonds. Adding oxygen-containing groups can boost catalytic activity and stability. Due to its hydrophilic properties, graphene oxide easily disperses in water and polar solvents [49, 50].
The synthesis of MOF-GO nanocomposites involves interactions between the oxygen groups of graphene oxide and the metallic centers of metal-organic frameworks, which occur through either chemical bonding or electrostatic interactions. To address its limitations, integrating MOF-199 with GO is considered essential [51]. The MOF-199/GO nanocomposites address several needs, including the capability for one-step synthesis, operation under ambient conditions, ease of catalyst recovery and recyclability, as well as effectiveness as adsorbents for RhB in wastewater treatment. This method aims to reduce environmental pollution.

2. Experimental

2.1 Materials

Graphite powder (> 99%), Potassium Chlorate ($KClO_3$) (> 99%), Sulfuric Acid (H_2SO_4) (> 99%), Nitric Acid (HNO_3) (> 99%), Methanol (> 99%) and Diethyl Ether (> 99%) were used for the synthesis of Graphene Oxide. $Cu(OAC)_2^{\bullet} H_2O$ (> 99%), 1,3,5-benzenetricarboxylate (BTC) (> 99%), Triethylamine (TEA) (> 99%), Dimethylformamide (> 99%), and Ethanol (> 99%) were used for the synthesis of MOF-199. Rhodamine B (> 99%) as dye, NaOH, and HCl were applied to vary the pH of the solutions.

2.2 Synthesis of GO

GO was prepared from pure graphite powder using the Staudenmaier method [52]. Initially, 1.0 g of graphite powder was combined with 17.0 mL of H_2SO_4 and 9.0 mL of fuming HNO_3 in a flat-bottom flask, which was then placed in an ice bath to ensure thorough mixing. Subsequently, 11.0 g of potassium chlorate was gradually added to the mixture over a 15-minute period. Following this reaction period, 800.0 mL of distilled water was introduced to the flask's contents, and the resulting suspension was subjected to filtration. The filtered material was washed with 5% hydrochloric acid, methanol, and diethyl ether until the pH of the filtrate was neutralized. After the washing process, the filtered material, designated as graphite oxide, was dried. A portion of this graphite oxide was then subjected to ultrasonication at 240 W for one hour to produce graphene oxide.

2.3 Preparation of MOF-199

In the experimental procedure, 500 mg (2.38 mmol) of benzene tricarboxylic acid was combined with 12 mL of a 1:1:1 mixture of DMF, ethanol, and water. Simultaneously, 860 mg (4.31 mmol) of copper (II) acetate monohydrate was mixed with 12 mL of the same solvent. The two solutions were combined under stirring conditions, and 0.5 mL of triethylamine was added to the reaction mixture, which was stirred for 23 h. The resulting product was washed with DMF [53].

2.4 Preparation of MOF-199/GO nanocomposite

MOF-199/GO prepared with the incorporation of GO with a content of 10 wt% to MOF-199. In the experimental procedure, 10 mg of graphene oxide was combined with 12 mL of a 1:1:1 mixture of DMF, ethanol, and water. After that, 500 mg (2.38 mmol) of benzene tricarboxylic acid was added to the solution. Simultaneously, 860 mg (4.31 mmol) of copper (II) acetate monohydrate was mixed with 12 mL of the same solvent. The two solutions were combined, and 0.5 mL of triethylamine was added to the solution. The resulting product washed with DMF.

2.5 Evaluation of photocatalytic activity

The efficacy of the MOF-199/GO nanocomposite photocatalyst for degrading Rhodamine B was evaluated under visible light using a 100 W lamp positioned 15 cm above the liquid surface. Photocatalyst concentrations of $0.005 - 0.05$ g/L were added to 100 mL of RhB aqueous solution at concentrations ranging from $2 - 10$ mg/L. The suspensions were magnetically stirred in the dark for 20 min to achieve adsorption-desorption equilibrium prior to illumination. The photocatalytic activity was quantified in terms of degradation efficiency, calculated based on the change in intensity of the absorption peak at 586 nm (λ_{max} of the dye) using a defined equation (1).

$$\text{Degradation}\% = 100\times\left[\frac{A_o - A_t}{A_o}\right] \quad (1)$$

For comparison, photocatalytic experiments involving pure MOF-199, GO, and a control without catalysts were conducted under identical conditions. To achieve optimal degradation efficiency, the concentrations of the dye were varied between 2 to 10 ppm, while the catalyst doses ranged from 0.01 to 0.2 g/L.

2.6 Characterization

The powder X-Ray diffraction (XRD) patterns of the samples were obtained using an X-Ray diffractometer (X Pert Pro MPD), employing Cu Kα radiation ($\lambda = 1.545$ Å) at operating conditions of 45 kV and 30 mA, with a step size of $2\theta = 0.02°$. Scans were conducted over a 2θ range of 2° to 70° at a rate of 2° min^{-1}, with all samples analyzed in random orientation. Transmission electron microscopy (TEM) images were captured using a Philips CM10 microscope, operating at an accelerating voltage of 100 kV. For TEM sample preparation, the powdered samples were dispersed in acetone by sonication before being drip-dried onto a copper grid coated with carbon film, followed by an additional 15 min of sonication. Scanning electron microscopy (SEM) analysis was performed with a TESCAN MIRA3 microscope at 30 kV. The specific surface area and pore diameter were assessed using a Sibata Surface Area Analyzer 1100, with samples degassed under vacuum at 180 °C for two h prior to measurement. Ultraviolet-visible diffused reflectance spectra (UV-Vis DRS) were collected using a UV-Vis Scinco 4100 spectrometer equipped with an integrating sphere reflectance accessory, with $BaSO_4$ serving as the reference material. Additionally, UV-Vis absorption

spectra were recorded using a Shimadzu 1600 PC spectrophotometer within the wavelength range of 190 – 900 nm. Fourier transform infrared (FT-IR) spectra were acquired on a Bruker spectrophotometer utilizing KBr pellets, with 128 scans taken in the spectral range of 4000 – 400 cm^{-1} at a resolution of 2 cm^{-1}; specifically, 0.5 mg of sample was mixed with 200 mg of KBr.

3. Results and discussion

3.1 Crystal pattern analysis

The XRD patterns of the MOF-199/GO nanocomposite, pure MOF-199, and Graphene oxide have been displayed in Fig. 2. From Fig. 2 (a), it shows a wide peak at $2\theta = 11.84°$ with the (001) hkl plane. This diffraction peak can be indexed to the hexagonal GO phase (JCPDS card No. 75-2078) [54]. GO typically contains some functional groups (OH, -COOH, etc.) along with water molecules. The presenting peak was created due to the presence of oxygen functional groups and water molecules within the carbon structure. Fig. 2 (b) shows apparent peaks at 6.89°, 9.69°, 11.84°, 13.49°, 17.54°, and 19.09°, which are attributed to the (200), (220), (222), (400), (511), and (600) reflections of MOF-199. These diffraction peaks can be indexed to the hexagonal MOF-199 phase (JCPDS card No. 23-00380) [55]. Fig. 2 (c) shows distinct peaks at 6.84°, 9.64°, 11.69°, 13.49°, 17.59° and 19.09° which reflections of MOF-199/GO. In comparison to the XRD pattern of pure metal organic framework, the diffraction pattern of the metal organic framework/graphene oxide composite does not exhibit any new absorption peaks. Both graphene oxide and MOF-199 exhibited peaks at approximately 11.84° in the X-ray diffraction (XRD) spectrum. In the nanocomposite synthesized from these materials, this peak is observed to be slightly shifted. Additionally, the intensity of this peak is lower in comparison to that of MOF-199 and higher compared to that of graphene oxide [53].

By using the Scherrer equation and peaks' width, the crystallite size (d) of the MOF-199/GO and the individual semiconductors was estimated. The MOF-199 and MOF-199/GO samples have average crystallite sizes of 110 nm and 220 nm, respectively. In the Scherrer equation (Eq. (2)), l shows the applied X-Ray wavelength (1.5406 Å), θ the Bragg angle, K the Scherrer constant (0.9), and β shows the full width at half maximum (FWHM) [56].

$$d = \frac{K\lambda}{\beta \cos\theta} \tag{2}$$

3.2 Analysis of electron microscopy images

Fig. 3 shows scanning electron microscope images of samples. The GO particles were in the range of ~ 2 to ~ 10 nm thickness and 200 nm -2 μm diameter. Graphen oxide exhibits a distinct layer structural arrangement (Fig. 3 (a)). The MOF-199 FE-SEM demonstrates cumulative of pyramidal shaped particles with average size of 200 nm (Fig. 3 (b)). The scanning electron microscope image of the nanocomposite particles shows metal organic framework particles are placed on the surface of GO nanosheets with aggregation

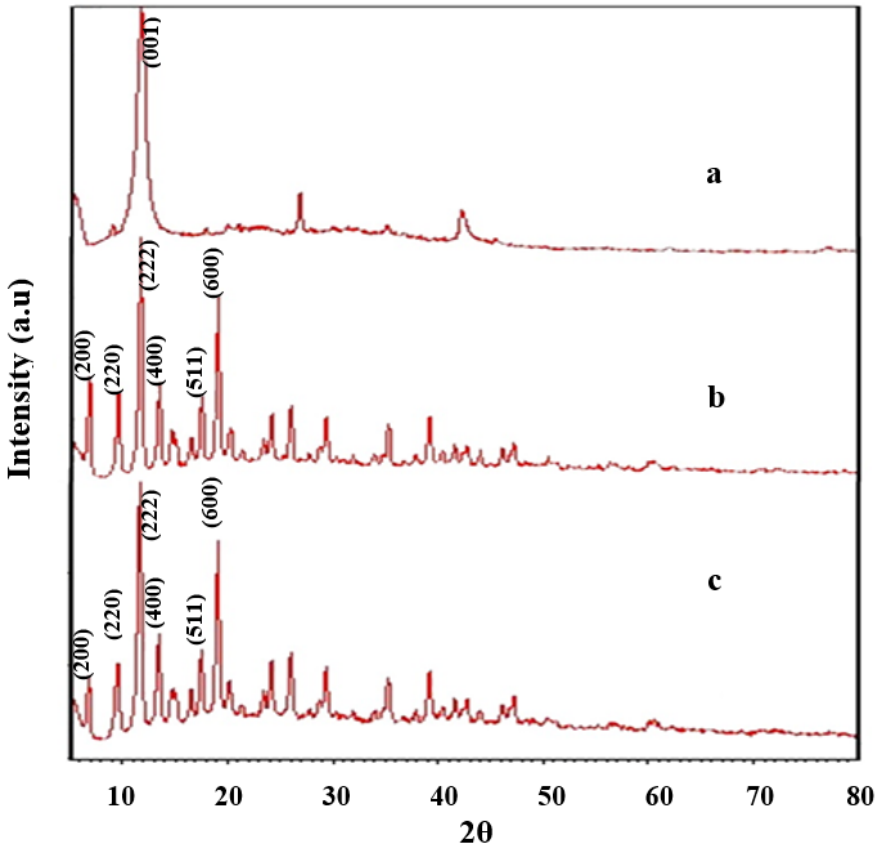

Figure 2. X-Ray diffractin patterns of (a) Graphene oxide, (b) MOF-199 metal organic framework, and (c) MOF-199/GO nanocomposite.

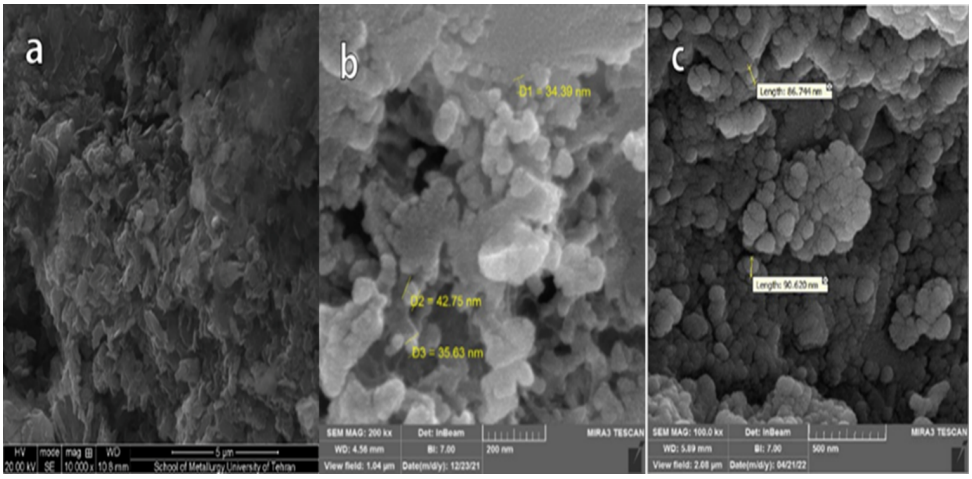

Figure 3. The scanning electron microscopy images of (a) GO, (b) MOF-199 metal organic framework, and (c) MOF-199/GO nanocomposite.

with average size of 90 nm (Fig. 3 (c)). Additionally, TEM images of GO (Fig. 4 (a)), MOF-199 (Fig. 4 (b)), and the MOF-199/GO composite (Fig. 4 (c)) are shown in (Fig. 4). The particles size was in agreements with SEM results.
EDX was employed as another effective analytical to thoroughly verify the successful synthesis of all steps of photocatalysts. Fig. 5 exhibits the EDX spectra of the synthesized sample. The EDX spectrum of MOF-199/GO showed the presence of copper, carbon, and oxygen (Fig. 5). The elemental mapping acquired by EDX further emphasized the successful distribution of MOF-199 in GO plates.

3.3 DRS and FTIR spectral analysis

The optical characteristics of MOF-199/GO photocatalyst, in conjunction with (GO), were analyzed using UV–vis DRS and the findings are represented in Fig. 6. You can see in Fig. 6, the absorption edge band of MOF-199 (Fig. 6 (a)) and MOF-199/GO (Fig. 6 (c)) indicated around 496 and 563 nm, respectively. This optical transition can be assigned to the interaction between organic ligands and Cu^{2+} center ions in MOF-199 [35]. The band gap energy of the samples is calculated according to the Tauc plot [57]. Based on the Tauc plot, the band gaps of MOF-199 and MOF-199/GO samples are approximately equivalent to 2.5 eV (Fig. 6 (b)) and 2.2 eV (Fig. 6 (d)), respectively. This enhanced absorption capacity resulted in a lower band gap for the GO/MOF199 nanocomposite, thereby improving its efficacy in visible light absorption. Accordingly, the GO/MOF199 nanocomposite is suggested as a promising photocatalyst for the degradation of RhB dye when subjected to visible light irradiation.
Fig. 7 presents the FT-IR spectrum of samples, which GO features a broad absorption peak around 3415 – 3565 cm^{-1} indicates the O-H stretching mode. This suggests the existence of hydroxyl groups in GO. Additionally, a distinct band observed at 1620 cm^{-1} is identified as characteristic of the carboxyl group, confirming the functionalization of the graphene oxide surface.
FT-IR spectrum of MOF-199 displays a broad absorption at 3448 cm^{-1}, which indicates O-H stretching from the solvent or hydrogen bonds. The peak at 1639 cm^{-1} can be attributed to C=O stretching from the carboxylate groups of 1,3,5-benzenetricarboxylate (BTC). The Peak at 1444 cm^{-1} is related to C=C stretching and may indicate aromatic character in the framework. The bands below 800 cm^{-1} correspond to metal-oxygen vibrations. In the analysis of the nanocomposite spectrum, all peaks characteristic of MOF-199 are identified. Notably, the peak corresponding of the region around 3400 cm^{-1} exhibits a slight shift, accompanied by an increase in intensity relative to that observed in MOF-199. This alteration can be attributed to the presence of -OH functional groups within the GO component.

3.4 Effect of photocatalytic experimental parameters

The influence of varying dosages of the MOF-199/GO photocatalyst on the photodegradation of RhB was analyzed within a concentration range of 0.01 to 0.2 g/L. The observed initial degradation rates increased with the photocatalyst dosage, reaching an optimal amount at 0.1 g/L of MOF-199/GO. Beyond this threshold, further increases in

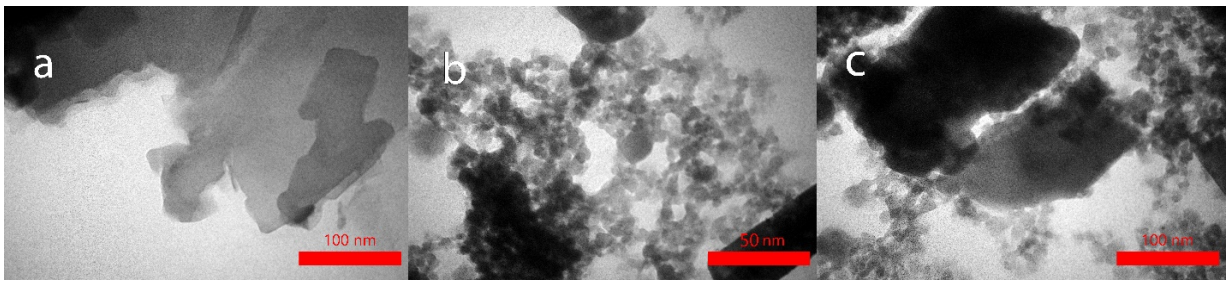

Figure 4. The transmission electron microscopy images of (a) GO, (b) MOF-0199 metal organic framework, and (c) MOF-199/GO nanocomposite.

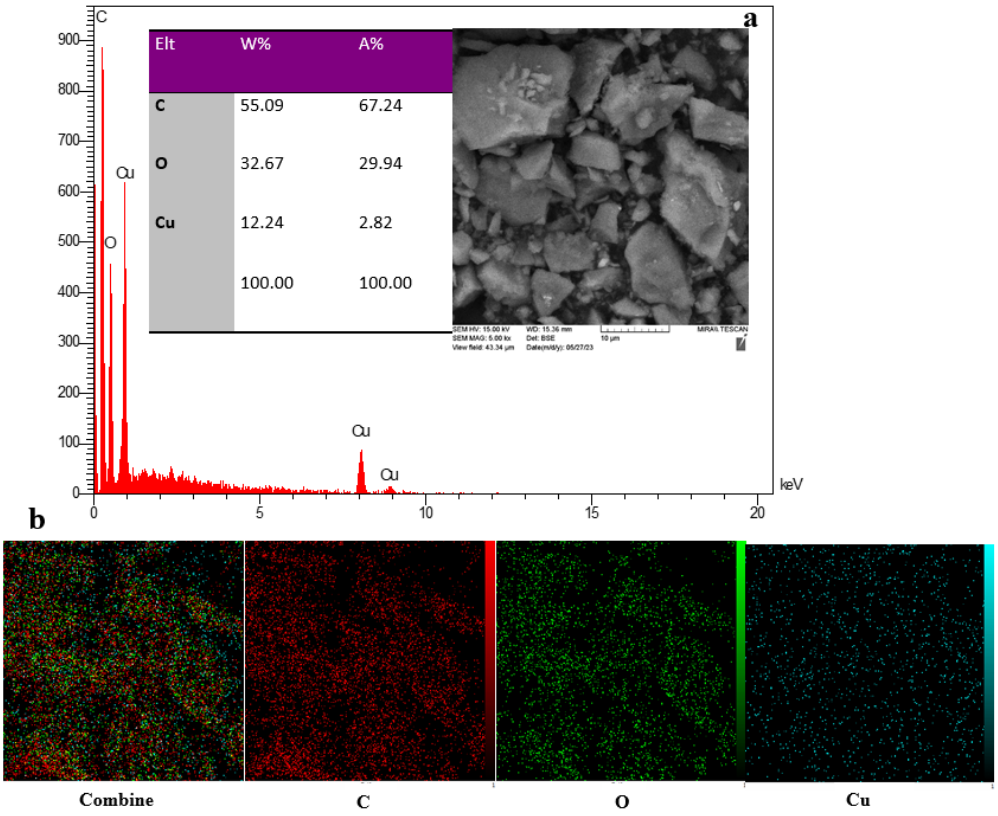

Figure 5. The EDX analysis (a) and elemental mapping (b) of the MOF-199/GO sample.

dosage did not yield additional benefits. While higher photocatalyst amounts facilitate increased dye adsorption on the catalytic surface, an excess may hinder light penetration into the solution, consequently diminishing the photodegradation rate due to particle aggregation [14].

The influence of initial Rhodamine B concentration on the rate of photocatalytic degradation was examined across a concentration range of 2 to 10 ppm. The results indicated

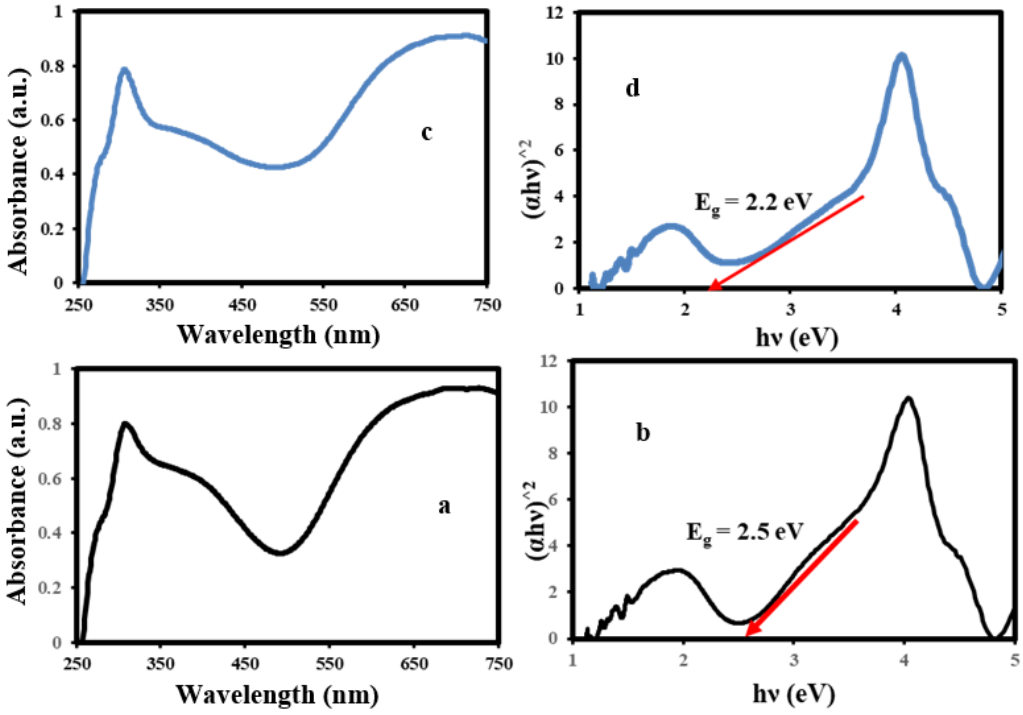

Figure 6. The DRS patterns and the Tauc plots (a, b) MOF-199 and (c, d) MOF-199/GO samples.

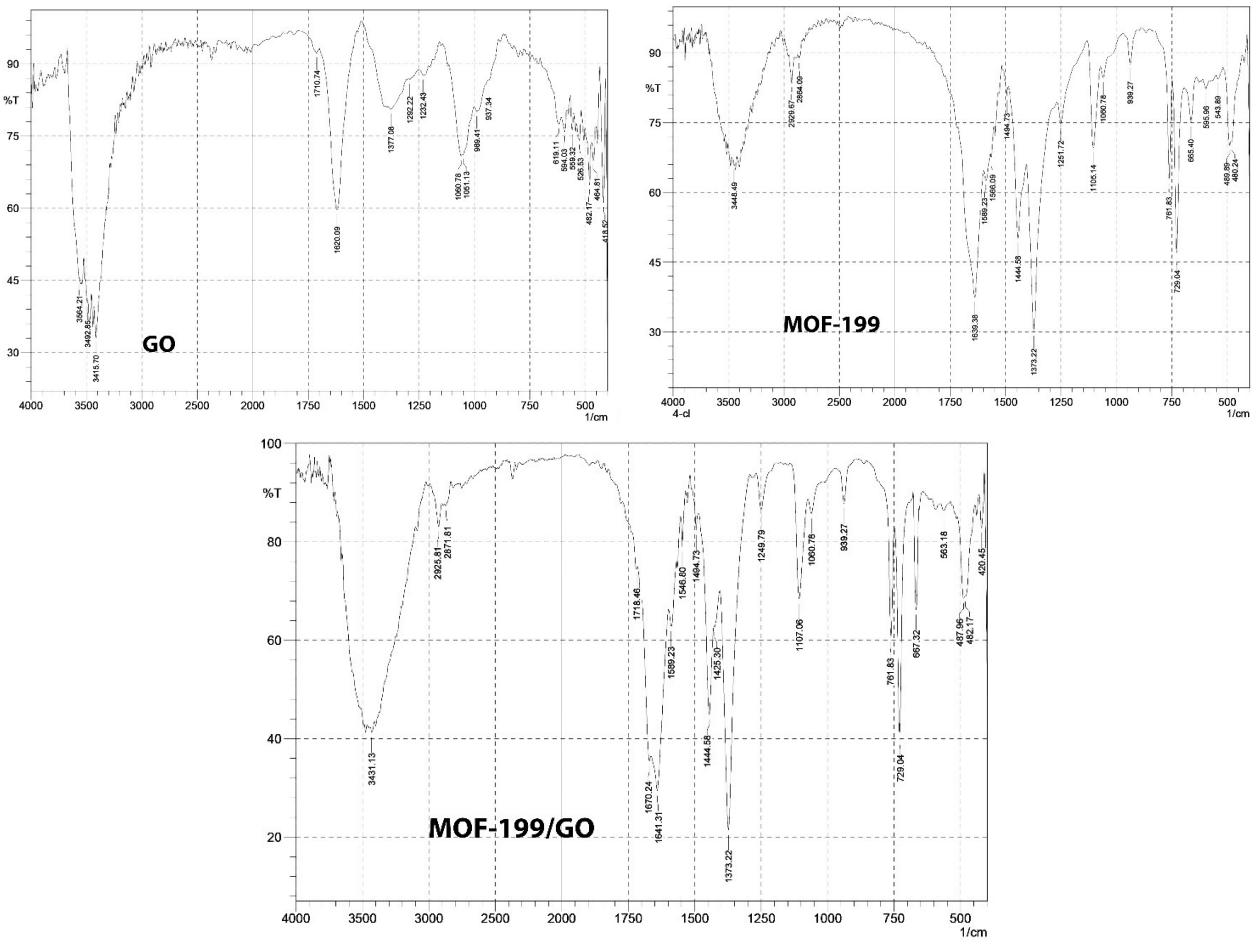

Figure 7. FTIR spectra of GO, MOF-199, and MOF-199/GO nanocomposite.

that dye degradation efficiency diminished as the initial concentration of Rhodamine B exceeded 5 ppm. At higher dye concentrations, the molecules significantly absorb light, limiting their availability to reach the photocatalyst surface. This reduction in light absorption by the photocatalyst directly correlates to a decrease in degradation efficiency [6]. The influence of various pH levels on the rate of photocatalytic degradation was examined across a pH range of 2 to 10. Furthermore, as the pH increases toward more alkaline conditions, the nanocomposite exhibits enhanced efficacy in both the adsorption and degradation of Rhodamine B from aqueous solutions. Conversely, at acidic pHs levels of 2 and 4, its performance is significantly diminished. On the other hand, the curve of ΔpH vs. initial pH obtained using the drift method for MOF-199/GO (Fig. 8). The pHpzc for MOF-199/GO was calculated to be 5.0. So, the surface of the synthesized nanocomposite had a negative charge in the pH experiment (neutral pH) range. The strong electrostatic attraction between RhB dye and the nanocomposite can be related to the negative and positive charges of the nanocomposite surface and RhB dye, respectively.

3.5 Photocatalytic degradation of Rhodamine B

The photocatalytic activity of the synthesized samples was evaluated using the Beer–Lambert law in an aqueous solution of dye under visible light irradiation. The photolysis conditions were assessed at a Rhodamine B concentration of 5 ppm and pH 8.5 for 60 min, revealing negligible degradation under these conditions. The degradation percentage of Rhodamine B, a cationic dye, in the presence of the synthesized photocatalysts was monitored within the wavelength range of 400 – 700 nm, as illustrated in Fig. 9.

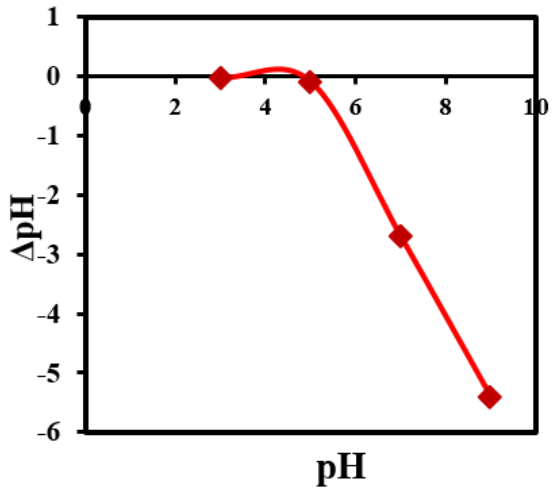

Figure 8. Graph of ΔpH versus initial pH obtained using the pH drift method in the presence of MoS_2@MOF 801 nanocomposite.

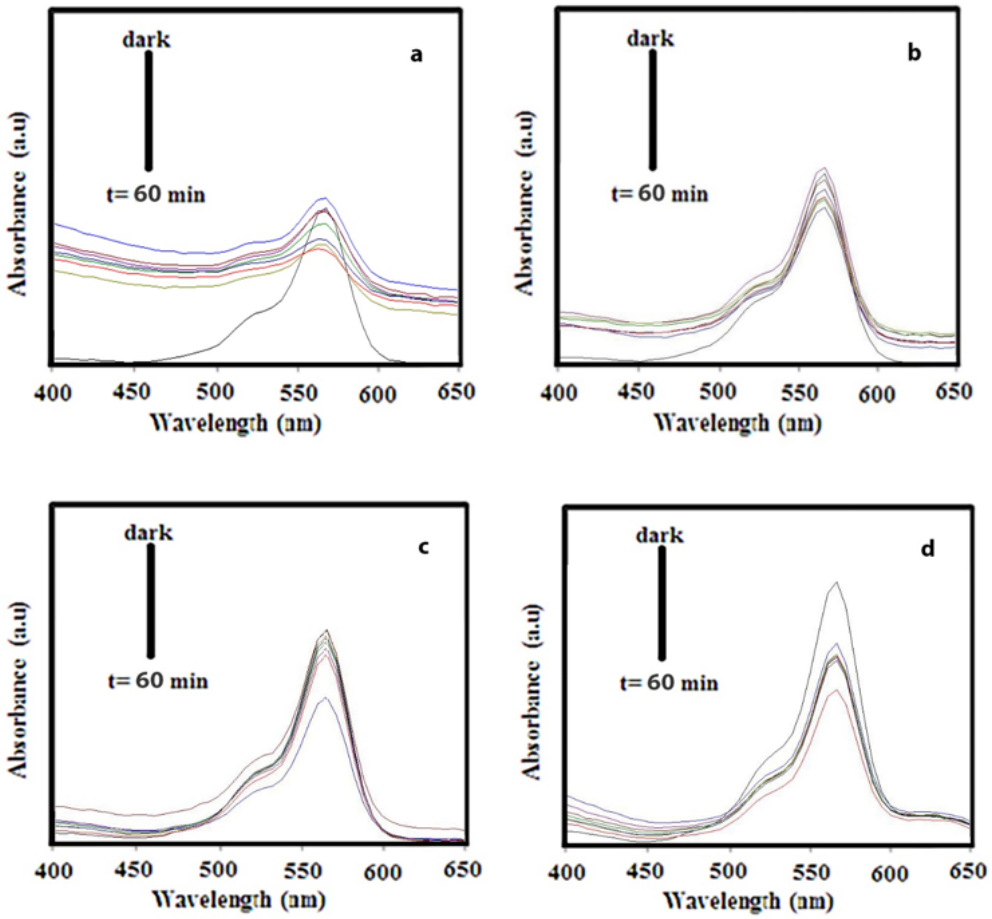

Figure 9. UV-vis absorption spectra of the Rhodamine B solution during the decomposition reaction under visible irradiation in the presence of (a) GO, (b) MOF-199 and (c) MOF-199/GO (Catalyst dosage: 0.1 g/L; initial conc. of dye: 5 mg/L; pH = 5.5) (d) MOF-199/GO (Catalyst dosage: 0.1 g/L; initial conc. of dye: 5 mg/L; pH = 8.5).

Magnetic stirring of the suspensions in the dark was conducted for 20 minutes to facilitate the establishment of an absorption-desorption equilibrium between the photocatalysts and Rhodamine B dye. The measured adsorption percentages for GO (Fig. 9 (a)), MOF-199 (Fig. 9 (b)), and the MOF-199/GO composite (Fig. 9 (c), (d)) were 9.6%, 7.8%, and 13.3%, respectively. The mechanisms of pollutant adsorption from wastewater using MOFs include acid-base interactions, electrostatic forces, hydrogen bonding, hydrophobic interactions, and $\pi - \pi$ stacking [19, 29]. Given the cationic nature of Rhodamine B, it is reasonable to anticipate electrostatic attraction between the catalysts and the dye. Particularly, GO, MOF-199, and MOF-199/GO demonstrated substantial Rhodamine B adsorption capacity, attributed to electrostatic interactions and $\pi - \pi$ interactions occurring between the benzene rings of Rhodamine B and the framework of MOF-199. Overall, the adsorption of dye on the surface samples is low, and this is a limitation for the synthesized catalyst with MOF-199 in its structure. The bulkiness of the ligand in the synthetic framework causes problems in dye adsorption due to steric hindrance.

In addition to adsorption mechanisms, organic dye pollutants can be effectively eliminated from wastewater through oxidative degradation facilitated by photocatalysts. The photodegradation efficiencies of Rhodamine B dye using GO, MOF-199, and MOF-199/GO were quantified at 21.5%, 19.9%, and 78.4%, respectively, after 60 min of visible-light irradiation under standardized conditions (dye concentration of 5 mg/L, photocatalyst dosage of 0.1 g/L, and pH 8.5) (Table 1). The MOF-199/GO composite exhibited the

Table 1. The photocatalytic performances of the photocatalysts, $C_0 = 5$ mg/L, the photocatalyst dosage: 0.1 g/L, pH = 8.5, at 20 min dark and 60 min under visible light irradiation.

Sample	Dye adsorption%	Dye degradation%	Dye removal%
GO	9.6	21.5	31.1
MOF-199	7.8	19.9	27.7
MOF-199/GO	13.3	78.4	91.7

highest catalytic activity among the samples tested. The superior photodegradation observed with MOF-199/GO is attributed to optimal interfacial contact between MOF-199 and the GO surface, minimizing particle aggregation, which is critical for enhancing photocatalytic performance.

To investigate the photostability of the synthesized MOF-199/GO photocatalyst, a series of five photocatalytic experimental runs was conducted. In each run, the previously used photocatalyst was added to a fresh dye solution without altering the overall concentration of the catalyst. After each cycle, the photocatalyst was reused following centrifugation, washed with double-distilled water, and dried at 80 °C, maintaining consistent conditions throughout. The photocatalytic activity of the nanocomposite was found to remain at approximately 80.7% even after five consecutive experimental runs. This retention of activity underscores the photocatalyst's potential for practical applications in environmental remediation. Therefore, the photocatalyst shows a favorable stability. The recovered photocatalyst was analyzed by XRD image in two angles (low and high angles) (Fig. 10 (a), (b)), the typical peaks of MOF-199 in the XRD pattern at low angle pattern ($2\theta = 5 - 10^0$) were observed better than the fresh nanocomposite (Fig. 2).

As presented in Fig. 10 (c), the photocatalytic abilities of the synthesized MOF-199/GO were compared with those of prepared MOF-199 and GO for the degradation of RhB under visible illumination. The plot of $\ln(C_0/C_t)$ vs time is linear resulting in rate constant (k) values of 0.0883, 0.0344, and 0.011 min^{-1}, obtained for MOF-199/GO, MOF-199 and GO samples, respectively (Fig. 10 (c)). The value of rate constant (k) for MOF-199/GO was more than other synthesized photocatalysts. The enhancement in the catalytic rate of MOF-199/GO could be attributed to facilitating the facile transfer of the photogenerated electrons to GO and reducing recombination e^-/h^+ in MOF-199.

3.6 Reaction mechanism

The adsorption of dye onto the surface and within the cavity of MOF-199/GO can be attributed to several factors, including electrostatic/ionic interactions, $\pi - \pi$ stacking interactions, and hydrogen bonding. It can be proposed that electrostatic attraction occurs between the positively charged RhB molecules and the negatively charged -OH groups present on the surface of the MOF-199/GO. Furthermore, MOF-199/GO nanocomposites offer several advantages, such as high surface area, varying functionalities,

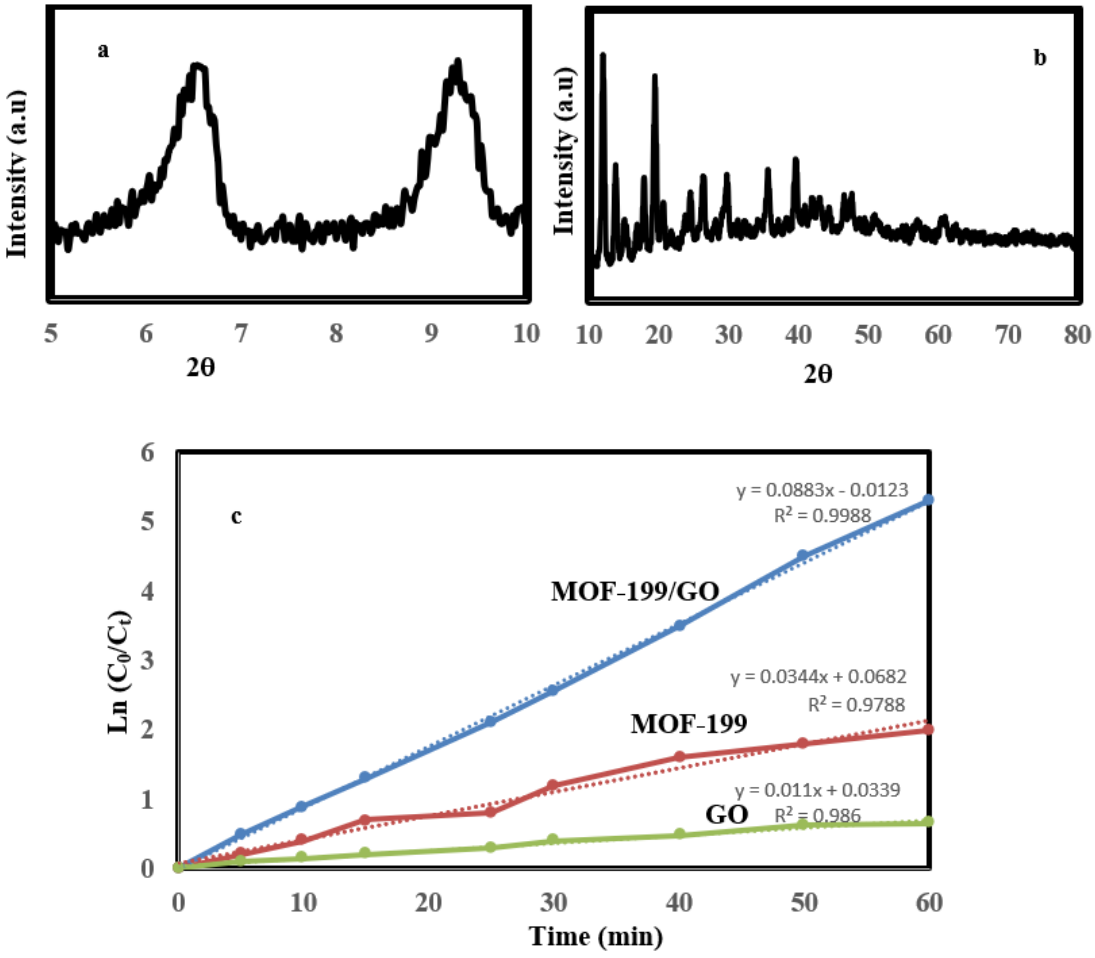

Figure 10. The XRD pattern of MOF-199/GO in (a) Low and (b) High angle after five photocatalytic experimental runs, and (c) The photocatalytic degradation curve or plots of C/C_0 vs time for the photodegradation of RhB using synthesized samples under the optimized conditions of the MOF-199/GO sample.

and tunable pore sizes. The adsorption mechanism of dye on MOF-199/GO can be attributed primarily to ionic interactions, which arise from the presence of unsaturated bonds (C=C, O=C=O) in the metal organic framework, the negatively charged surface of graphene oxide (GO), and the positive charge of dye. Additionally, $\pi-\pi$ interactions contribute significantly as active binding sites for the dye molecule within the MOF-199/GO matrix. Given that RhB contains C=C double bonds and $\pi-$ electrons, these $\pi-$ electrons are capable of engaging with the $\pi-$ electrons of the benzene rings present on both the metal organic framework and graphene oxide surfaces via $\pi-\pi$ interactions. Therefore, it can be inferred that the RhB is readily adsorbed on the MOF-199/GO surface. In this work, the RhB dye has the ability to be absorbed onto both species, MOF-199 and GO. However, in the RhB dye degradation process, the MOF-199 plays the role of a semiconductor, and by irradiating light to the nanocomposite, electrons/-holes are produced in the MOF-199. Graphene was used to prevent electron-hole recombination in the MOF-199.

In order to explain the mechanism of enhanced photocatalytic activity, trapping experiments involving different reactive radical species for RhB degradation over MOF-199/GO nanocomposite were first performed. In this study, three different chemicals, including disodium ethylenediaminetetraacetate (Na_2EDTA), p-benzoquinone (BZQ), and isopropanol (IPA), were used as scavengers for photogenerated holes (h^+), superoxide anion radicals ($^\bullet O_2^-$), and hydroxyl radicals ($^\bullet OH$), respectively. As shown in Table 2, a fast deactivation of the MOF-199/GO photocatalyst was observed for the addition of EDTA and BZQ, which reduced the diazinon degradation from almost 78.4% to 70.3% and 69.7% in 60 min. The results confirm that photocatalysis can be influenced by h^+ and $^\bullet O_2^-$. However, the presence of IPA shows a weak inhibition of photocatalytic activity. Herein, a Z-scheme mechanism for the efficient photocatalytic activity of the MOF-199/GO is proposed according to the above results.

Table 2. The photogenerated active species are trapped in the system of photodegradation of RhB by the MOF-199/GO photocatalyst under visible light irradiation.

Sample	IPA ($^\bullet OH$)	BZQ ($^\bullet O_2^-$)	EDTA (h^+)	No scavenger
%Degradation of MOF-199/GO	25.3	69.7	70.3	78.4

The proposed mechanism of photodegradation is presented in Fig. 10. As illustrated in Fig. 11, photogenerated electrons and holes can be generated in MOF-199 under visible light irradiation due to its narrow band gap. The electrons are then transferred from MOF-199 to the GO of MOF-199/GO and the holes remin on the MOF-199. Consequently, the electrons that accumulate on the GO can effectively reduce oxygen to form the reactive $^\bullet O_2^-$ species [$(O_2/^\bullet O_2^-) = -0.28$ eV vs. SHE], and the holes that remain on the MOF-199 can directly oxidize RhB molecules or oxidize water molecules to form $^\bullet OH$ species [$(^\bullet OH/H_2O) =$ 2.27 eV vs. SHE] [8]. Thus, the Z-scheme not only reduces

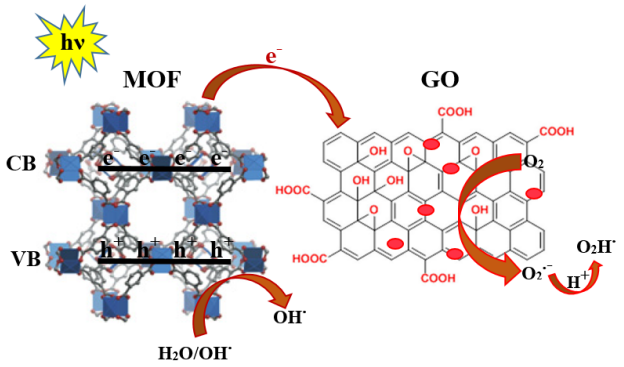

Figure 11. Proposed mechanism for the photocatalytic activity of the nanocomposite under visible light.

the electron–hole pair recombination but also possesses considerably strong oxidation and reduction ability as well. In other words, these results confirm the efficient photocatalytic activity and stability of MOF-199/GO nanocomposite.

To evaluate the RhB degradation by the synthesized photocatalyst in the oxidation process, the results from this study were compared with other reported metal-organic framework catalysts in the literature (Table 3). Comparing our work with other works shows that the low amount of synthesized photocatalyst has shown good degradation, but the time consumed to destroy the sample is relatively long. If a nano-particle were loaded in the photocatalyst, the time of degradation would be reduced, but the presence of bulk linker in the structure prevented nanoparticles from being synthesized.

4. Conclusion

A novel MOF-199/GO nanocomposite was successfully synthesized for the effective removal of RhB. The formation of the MOF-199/GO composite is attributed to electrostatic interactions between the positively charged metal centers of the metal organic framework and the negatively charged surface of GO. These nanocomposites exhibit excellent adsorption capacity for dye. The morphology of dye-adsorbed MOF-199/GO indicates the presence of irregularly shaped metal-organic framework nanoparticles ranging in size from 35 to 200 nm. EDS analyses confirmed the presence of carbon, oxygen, and copper clusters. One significant advantage of MOF-199/GO in dye degradation, compared to other photocatalysts, is its desired degradation time of 60 minutes and a minimal catalyst dosage of 0.1 g/L. The percentage of photocatalytic removal of Rhodamine B by MOF-199/GO nanocomposites was determined to be 91.7% at a concentration of 5 ppm and pH 8.5.

Acknowledgment

The authors are grateful to the Islamic Azad University, Rasht Branch.

Table 3. Comparison of the photocatalytic performance of the MOF-199/GO nanocomposite with reported literature data.

Catalyst	Dye, concentration	Amount (g/L)	Time (h)	Degradation (%)	Ref.
UiO-66	RhB, 0.03 mM	5	0.25	7	58
Fe_3O_4@MIL-100(Fe)	MB, 40 mg/L	0.1	1	99	59
Carbonized CuBTC	RhB, 25 mg/L	11	0.075	98	60
	MB, 18.5 mg/L	12	0.05	99	60
BiOBr/UiO-66	RhB, 0.03 mM	5	0.25	95	58
MIL-53 (Fe)	MB, 4×10^{-4} M	0.1	1	17	61
	MB, 4×10^{-4} M	0.1	0.5	99	61
MOF-199/GO	RhB, 5 mg/L	0.1	1	92	This work

Authors contributions
Authors have contributed equally in preparing and writing the manuscript.

Availability of data and materials
The data that support the findings of this study are available from the corresponding author, upon reasonable request.

Conflict of interests
The author declare that they have no known competing financial interests or personal relationships that could have appeared to influence the work reported in this paper.

References

[1] Sh. Sohrabnezhad and A. Pourahmad. *Electroanalysis*, **19**(2007): 1635–1641.
DOI: https://doi.org/10.1002/elan.200703898.

[2] Sh. Sohrabnezhad, A. Pourahmad, and M. Razavi. *Appl. Phys. A*, **122**(2016):1–9.
DOI: https://doi.org/10.1007/s00339-016-0349-4.

[3] A. Pourahmad and M. Deljoopour. *SYN REACT INORG METAORG NANOMETAL CHEM*, **46**(2016):694–700.
DOI: https://doi.org/10.1080/15533174.2014.989578.

[4] H. Derikvandi and A. Nezamzadeh-Ejhieh. *Solid State Sci.*, **101**(2020):106127.
DOI: https://doi.org/10.1016/j.solidstatesciences.2020.106127.

[5] A. Pourahmad. *Synth. React. Inorg. Met.-Org. Chem.*, **45**(2015): 1080–1086, .
DOI: https://doi.org/10.1080/15533174.2013.862656.

[6] Sh. Ghattavi and A. Nezamzadeh-Ejhieh. *Compos. B Eng.*, **183**(2020):107712.
DOI: https://doi.org/10.1016/j.compositesb.2019.107712.

[7] A. Albouyeh, A. Pourahmad, and K. Kefayati. *J. Coord. Chem.*, **74**(2021):2174–2184, .
DOI: https://doi.org/10.1080/00958972.2021.1954173.

[8] A. Pourahmad and F. Azadi. *J. Coord. Chem.*, **75**(2022):2136–2149.
DOI: https://doi.org/10.1080/00958972.2022.2124862.

[9] L. Jafari, A. Pourahmad, and L. Asadpour. *INORG NANO-MET CHEM.*, **47**(2017):1552–1559.
DOI: https://doi.org/10.1080/24701556.2017.1357609.

[10] A. Yousefi and A. Nezamzadeh-Ejhieh. *Iran. J. Catal.*, **11**(2021): 247–259. URL https://oiccpress.com/ijc/article/view/3600.

[11] F. Eshghi, Z. Mehrabadi, et al. *Environ. Res.*, **222**(2023):115321.
DOI: https://doi.org/10.1016/j.envres.2023.115321.

[12] A. Pourahmad. *Arab. J. Chem.*, **7**(2014):788–792, .
DOI: https://doi.org/10.1016/j.arabjc.2011.07.018.

[13] S. Zinatloo-Ajabshir, S. Rakhshani, et al. *J. Environ. Manag.*, **350**(2024):119545, .
DOI: https://doi.org/10.1016/j.jenvman.2023.119545.

[14] S. Zinatloo-Ajabshir, Z. Mehrabadi, H. Khojasteh, and F. Sharifianjazi. *Ceram. Int.*, **50**(2024):49263–49276, .
DOI: https://doi.org/10.1016/j.ceramint.2024.09.271.

[15] J. Li, H. Wang, X. Yuan, J. Zhang, and J. W. Chew. *Coord. Chem. Rev.*, **404**(2020):213116, .
DOI: https://doi.org/10.1016/j.ccr.2019.213116.

[16] G. Kumar and D. T. Masram. *ACS Omega.*, **6**(2021):9587–9599.
DOI: https://doi.org/10.1021/acsomega.1c00143.

[17] A. Pourahmad and Sh. Sohrabnezhad. *Mater. Let.*, **65**(2011):205–207.
DOI: https://doi.org/10.1016/j.matlet.2010.10.009.

[18] K. Ventura, R. A. Arrieta, M. Marcos-Hernández, V. Jabbari, C. D. Powell, R. Turley, A. W. Lounsbury, J. W. Zimmerman, J. Gardea-Torresdey, M. S. Wong, and D. Villagrán. *Sci. Total Environ.*, **738**(2020):139213.
DOI: https://doi.org/10.1016/j.scitotenv.2020.139213.

[19] S. Luo, J. Wang, and Environ. *Sci. Pollut. Res. Int.*, **25**(2018):5521–5528.
DOI: https://doi.org/10.1007/s11356-017-0932-z.

[20] A. Albouyeh, A. Pourahmad, and H. kefayati. *J Water Environ Nanotechnol*, **5**(2020):283–293, .
DOI: https://doi.org/10.22090/jwent.2020.03.008.

[21] Q. Al-Naddaf, M. Al-Mansour, H. Thakkar, and F. Rezaei. *Ind. Eng. Chem. Res.*, **57**(2018):17470–17479.
DOI: https://doi.org/10.1021/acs.iecr.8b03638.

[22] M. Muschi, S. Devautour-Vinot, D. Aureau, N. Heymans, S. Sene, R. Emmerich, et al. *J. Mater. Chem. A*, **9**(2021):13135–13142.
DOI: https://doi.org/10.1039/D0TA12215G.

[23] B. Azari, A. Pourahmad, B. Sadeghi, and M. Mokhtary. *J. Coord. Chem.*, **76**(2023):219–231.
DOI: https://doi.org/10.1080/00958972.2023.2166408.

[24] Z. U. Zango, K. Jumbri, N. S. Sambudi, A. Ramli, H. H. Abu Bakar, B. Saad, et al. *Polymers*, **12**(2020):2648.
DOI: https://doi.org/10.3390/polym12112648.

[25] E. Rahimi and N. Mohaghegh. *Environ. Sci. Pollut. Res.*, **24**(2017): 22353–22360.
DOI: https://doi.org/10.1007/s11356-017-9823-6.

[26] F. Azadi, A. Pourahmad, Sh. Sohrabnezhad, and M. Nikpassand. *J. Coord. Chem.*, **73**(2020):3412–3419.
DOI: https://doi.org/10.1080/00958972.2020.1858481.

[27] B. Paulchamy, G. Arthi, and B. D. Lignesh. *J. Nanomed. Nanotechnol.*, **6**(2015):100253.
DOI: https://doi.org/10.4172/2157-7439.1000253.

[28] P. Ranjan, S. Agrawal, A. Sinha, T. R. Rao, J. Balakrishnan, and A. D. Thakur. *Sci. Rep.*, **8**(2018):12007. URL https://www.nature.com/articles/s41598-018-30613-4.

[29] Y. Bao, Q. Yan, J. Ji, and B. Qiu. *Trans. Tianjin Univ.*, **27**(2021):110–126.
DOI: https://doi.org/10.1007/s12209-020-00276-2.

[30] S. Y. Lee, D. Kang, S. Jeong, H. T. Do, and J. H. Kim. *ACS Omega.*, **5**(2020):4233–4241.
DOI: https://doi.org/10.1021/acsomega.9b04127.

[31] D. Pattappan, S. Vargheese, K. V. Kavya, R. T. Rajendra Kumar, and Y. Haldorai. *Chemosphere*, **286**(2020):131726.
DOI: https://doi.org/10.1016/j.chemosphere.2021.131726.

[32] J. Glover and E. Besley. *Faraday Discuss*, **231**(2021):235–257.
DOI: https://doi.org/10.1039/D1FD00005E.

[33] P. Sivakumar and P. N. Palanisamy. *Int. J. ChemTech Res.*, **1**(2009):502–510.

[34] S. D. Ashrafi, S. Rezaei, H. Forootanfar, A. H. Mahvi, and M. A. Faramarzi. *Int. Biodeterior. Biodegrad.*, **85**(2013):173–181.
DOI: https://doi.org/10.1016/j.ibiod.2013.07.006.

[35] E. Bazrafshan, F. K. Mostafapour, A. R. Hosseini, A. Raksh Khorshid, and A. H. Mahvi. *J. Chem.*, **2013**(2012):1–8.
DOI: https://doi.org/10.1155/2013/938374.

[36] S. S. Mirzadeh, S. M. Khezri, S. Rezaei, H. Forootanfar, A. H. Mahvi, and M. A. Faramarzi. *J. Environ. Health Sci. Eng.*, **12**(2014).
DOI: https://doi.org/10.1186/2052-336x-12-6.

[37] A. Dalvand, R. Nabizadeh, M. R. Ganjali, and M. Khoobi. *J. Magn. Magn. Mater.*, **404**(2016):179–189.
DOI: https://doi.org/10.1016/j.jmmm.2015.12.040.

[38] N. K. Mogha, S. Gosain, and D. T. Masram. *Appl. Surf. Sci.*, **396**(2017):1427–1434.
DOI: https://doi.org/10.1016/j.apsusc.2016.11.182.

[39] A. Mariyam, M. Shahid, I. Mantasha, M. Shahnawaz Khan, and M. Shahwaz Ahmad. *J. Inorg. Organomet. Polym. Mater.*, **30**(2019):1–9.
DOI: https://doi.org/10.1007/s10904-019-01334-6.

[40] C. Janiak and J. K. Vieth. *New J. Chem.*, **34**(2010):2366–2388.
DOI: https://doi.org/10.1039/C0NJ00275E.

[41] Y. Wang, C. Hou, Y. Zhang, F. He, M. Liu, and X. Li. *J. Mater. Chem. B*, **4**(2016):3695–3702.
DOI: https://doi.org/10.1039/C6TB00276E.

[42] D. R. Dreyer, S. Park, C. W. Bielawski, and R. S. Ruoff. *Chem. Soc. Rev.*, **39**(2010):228–240.
DOI: https://doi.org/10.1039/B917103G.

[43] J. Zhu, D. Yang, Z. Yin, Q. Yan, and H. Zhang. *Small*, **10**(2014):3480–3498.
DOI: https://doi.org/10.1002/smll.201303202.

[44] W. Fan, X. Wang, B. Xu, Y. Wang, D. Liu, M. Zhang, Y. Shang, F. Dai, L. Zhang, and D. Sun. *J. Mater. Chem. A*, **2018**(2018):24486–24495.
DOI: https://doi.org/10.1039/C8TA07839D.

[45] L. Brinda, K. S. Rajan, and J. B. B. Rayappan. *J. Appl. Sci.*, **12**(2012):1778–1780.
DOI: https://doi.org/10.3923/jas.2012.1778.1780.

[46] O. M. Yaghi, M. O'Keeffe, N. W. Ockwig, H. K. Chaet, M. Eddaoudi, and J. Kim. *Nature*, **423**(2003):705–714.
DOI: https://doi.org/10.1038/nature01650.

[47] M. Z. Iqbal, M. Shaheen, M. W. Khan, S. Siddique, S. Aftab, S. M. Wabaidur, and M. J. Iqbal. *RSC Adv.*, **13**(2023):2860–2870, .
DOI: https://doi.org/10.1039/D2RA06457J.

[48] L. Giraldo, M. Bastidas-Barranco, P. Húmpola, and J. C. Moreno-Piraján. *Eur. J. Chem.*, **8**(2017):293–304.
DOI: https://doi.org/10.5155/eurjchem.8.3.293-304.1603.

[49] Q. Li, F. Fan, Y. Wang, W. Feng, and P. Ji. *Ind. Eng. Chem. Res.*, **52**(2013):6343–6348, .
DOI: https://doi.org/10.1021/ie400558u.

[50] L. Liao, Y. Gao, S. Zhu, J. Zheng, Z. Chen, C. Yin, X. Lou, and D. Zhang. *ACS Appl. Mater. Interfaces*, **7**(2015):19619–19625.
DOI: https://doi.org/10.1021/acsami.5b05649.

[51] C. Petit and T. J. Bandosz. *Adv. Mater.*, **21**(2009):4753–4757.
DOI: https://doi.org/10.1002/adma.200901581.

[52] S. N. Alam, N. Sharma, and L. Kumar. *Graphene*, **6**(2017):1–18.
DOI: https://doi.org/10.4236/graphene.2017.61001.

[53] N. M. Mahmoodi and J. Abdi. *Microchem. J.*, **144**(2019):436–442.
DOI: https://doi.org/10.1016/j.microc.2018.09.033.

[54] D. C. Marcano, D. V. Kosynkin, et al. *ACS Nano*, **4**(2010):4806–4814.
DOI: https://doi.org/10.1021/nn1006368.

[55] M. Z. Iqbal, M. Shaheen, et al. *RSC Adv.*, **13**(2023):2860–2870, .
DOI: https://doi.org/10.1039/D2RA06457J.

[56] F. Soleimani and A. Nezamzadeh-Ejhieh. *J. Mater. Rea. Technol.*, **9**(2020):16237–16251.
DOI: https://doi.org/10.1016/j.jmrt.2020.11.091.

[57] N. Mehrabanpour, A. Nezamzadeh-Ejhieh, Sh. Ghattavi, and A. Ershadi. *Appl. Surf. Sci.*, **614**(2023):156252.
DOI: https://doi.org/10.1080/00958972.2021.1954173.